



Semi-discrete central-upwind Rankine-Hugoniot schemes for hyperbolic systems of conservation laws

Naveen Kumar Garg^{a,b}, Alexander Kurganov^c, Yongle Liu^{d,a,*}

^a Department of Mathematics, Southern University of Science and Technology, Shenzhen, 518055, China

^b IISc Mathematics Initiative (IMI), Indian Institute of Science, Bangalore, 560012, India

^c Department of Mathematics and SUSTech International Center for Mathematics, Southern University of Science and Technology, Shenzhen, 518055, China

^d Department of Mathematics, Harbin Institute of Technology, Harbin, 150001, China



ARTICLE INFO

Article history:

Received 30 June 2020

Received in revised form 18 October 2020

Accepted 10 December 2020

Available online 6 January 2021

Keywords:

Central-upwind schemes

Discrete Rankine-Hugoniot conditions

Numerical dissipation switch

Local speeds of propagation

Euler equations of gas dynamics

ABSTRACT

We study semi-discrete central-upwind schemes and develop a new technique that allows one to decrease the amount of numerical dissipation present in these schemes without compromising their robustness. The goal is achieved by obtaining more accurate estimates for the one-sided local speeds of propagation using the discrete Rankine-Hugoniot conditions. In the two-dimensional case, these estimates are further enhanced with the help of the numerical dissipation switch mechanism, which is automatically activated near contact discontinuities and shear layers. The resulting central-upwind Rankine-Hugoniot schemes are tested on a number of numerical examples for both the one- and two-dimensional Euler equations of gas dynamics. The obtained results clearly demonstrate the superiority of the proposed method over the existing semi-discrete central-upwind schemes.

© 2020 Elsevier Inc. All rights reserved.

1. Introduction

In this paper, we focus on the numerical solutions of hyperbolic systems of conservation laws, which in one-dimensional (1-D) case read as

$$\mathbf{U}_t + \mathbf{F}(\mathbf{U})_x = \mathbf{0}, \quad (1.1)$$

where x is a spatial variable, t is time, $\mathbf{U}(x, t) \in \mathbb{R}^N$ is a vector of conserved variables, and \mathbf{F} is a flux vector. It is well-known that solving (1.1) numerically can be a daunting task, as these systems may develop complicated nonsmooth structures including shock waves, rarefactions, and contact discontinuities even for sufficiently smooth initial data. It is therefore quite challenging to develop robust and highly accurate numerical methods to capture such features. In order to gain both robustness and accuracy, these methods must have a sufficient but not excessive amount of built-in numerical diffusion. Typically, finite-volume Godunov-type schemes provide a popular framework to achieve this goal; see, e.g., the monographs [7,12,15,25]. Here, we would like to recall that in the framework of Godunov-type schemes, the solution is represented in terms of its cell averages. They are used to obtain a global in space piecewise polynomial reconstruction, which is then evolved in time using the integral form of the studied system of conservation laws.

* Corresponding author.

E-mail addresses: garg.naveen70@gmail.com (N.K. Garg), alexander@sustech.edu.cn (A. Kurganov), liyli2017@mail.sustech.edu.cn (Y. Liu).

Godunov-type schemes can be further divided into two major categories: *upwind* and *central* ones. The first stable upwind scheme is the Godunov scheme proposed in [8]. It is based on solving the Riemann problems at all of the cell interfaces at every time step. Higher-order finite-volume methods employ higher-order piecewise polynomial reconstructions. Therefore, in order to develop higher-order upwind methods one needs to (approximately) solve the generalized Riemann problems, which is a much more complicated task; see, e.g., [3] and references therein. On the other hand, in Godunov-type central schemes, no (generalized) Riemann problem solver is required for time evolution. This makes central schemes much simpler to apply to a wide variety of hyperbolic systems of conservation laws as “black-box” solvers; see, e.g., [16] and references therein. The simplest Godunov-type central scheme is the first-order staggered Lax-Friedrichs scheme whose order and hence resolution can be increased upon using proper piecewise polynomial reconstructions. This way the Nessyahu-Tadmor scheme [32], its higher-order [4,26,31,34] and multi-dimensional [1,2,14,27,28] extensions were derived.

Due to the staggered grid structure, staggered central schemes have quite a large amount of numerical dissipation, which can be reduced by utilizing the information about the one-sided local speeds of propagation. This was done in [20,22,23], where nonstaggered *central-upwind* (CU) schemes were developed. The CU schemes are not only more accurate but also more robust than the staggered ones, as the numerical diffusion coefficients in the CU schemes are not inversely proportional to the size of the time step; see [22] for detailed analysis. The CU schemes were further developed in [17,18,21], where a considerable amount of numerical dissipation present in the original CU schemes was removed.

The CU schemes, however, are still more dissipative than their upwind counterparts, particularly near contact discontinuities. Here, we aim to further reduce the amount of numerical dissipation present in the CU schemes without compromising their robustness. In order to achieve this goal, we obtain more accurate estimates of one-sided local speeds of propagation and hence perform a more accurate time evolution of the computed solution. To this end, we implement the approach introduced in central Rankine-Hugoniot (R-H) schemes [6,13,35,41], in which the amount of numerical dissipation is controlled mostly by the *discrete R-H conditions* near/at steady discontinuities. We call the resulting scheme central-upwind Rankine-Hugoniot (CURH) scheme. In the two-dimensional (2-D) case, we further reduce the amount of numerical dissipation by implementing the *numerical dissipation switch* mechanism recently introduced in [33], and then modified in [18,19]. The main idea of this mechanism is to locally reduce the influence of the acoustic wave speeds in the directions tangent to the dominating direction of the fluid flows near/at contact waves and shear layers.

The paper is organized as follows. We first briefly review the 1-D CU schemes in §2.1 and then derive the 1-D CURH scheme in §2.2. The 2-D numerical dissipation switch mechanism is reviewed in §3.1. It is then used to develop the 2-D CURH scheme in §3.2. Finally, we test the proposed CURH schemes and compare their performance with the previous versions of the CU schemes on several numerical examples for both 1-D (§4.1) and 2-D (§4.2) Euler equations of gas dynamics.

2. One-dimensional central-upwind Rankine-Hugoniot (CURH) scheme

In this section, we first present a brief overview of the CU schemes in §2.1 and then provide a detailed description on how to more accurately estimate the one-sided local speeds propagation near/at the contact waves. This would lead to the CURH scheme in §2.2.

2.1. The second-order semi-discrete central-upwind (CU) schemes: a brief overview

Here, a brief description of the second-order semi-discrete CU schemes for (1.1) from [17] is provided. Let us split the computational domain into the finite-volume cells $C_j := [x_{j-\frac{1}{2}}, x_{j+\frac{1}{2}}]$, which, for the sake of brevity, are assumed to be uniform so that $x_{j+\frac{1}{2}} - x_{j-\frac{1}{2}} \equiv \Delta x$ for all j .

As in all finite-volume methods, the computed solution is realized in terms of its cell averages $\bar{\mathbf{U}}_j(t) \approx \frac{1}{\Delta x} \int_{C_j} \mathbf{U}(x, t) dx$. They are assumed to be known at a given time t , and are then evolved in time according to the following semi-discretization:

$$\frac{d}{dt} \bar{\mathbf{U}}_j = -\frac{\mathcal{F}_{j+\frac{1}{2}} - \mathcal{F}_{j-\frac{1}{2}}}{\Delta x}. \quad (2.1)$$

Here, $\mathcal{F}_{j+\frac{1}{2}}$ is the CU numerical flux which was originally derived in [20,22] and later modified in [17]:

$$\mathcal{F}_{j+\frac{1}{2}} = \frac{a_{j+\frac{1}{2}}^+ \mathbf{F}(\mathbf{U}_j^E) - a_{j+\frac{1}{2}}^- \mathbf{F}(\mathbf{U}_{j+1}^W)}{a_{j+\frac{1}{2}}^+ - a_{j+\frac{1}{2}}^-} + \frac{a_{j+\frac{1}{2}}^+ a_{j+\frac{1}{2}}^-}{a_{j+\frac{1}{2}}^+ - a_{j+\frac{1}{2}}^-} \left[\mathbf{U}_{j+1}^W - \mathbf{U}_j^E - \delta \mathbf{U}_{j+\frac{1}{2}} \right]. \quad (2.2)$$

The built-in “anti-diffusion” term $\delta \mathbf{U}_{j+\frac{1}{2}}$ is given by

$$\delta \mathbf{U}_{j+\frac{1}{2}} = \text{minmod} \left(\mathbf{U}_{j+1}^W - \mathbf{U}_{j+\frac{1}{2}}^*, \mathbf{U}_{j+\frac{1}{2}}^* - \mathbf{U}_j^E \right), \quad (2.3)$$

where

$$\mathbf{U}_{j+\frac{1}{2}}^* = \frac{a_{j+\frac{1}{2}}^+ \mathbf{U}_{j+1}^W - a_{j+\frac{1}{2}}^- \mathbf{U}_j^E - \{\mathbf{F}(\mathbf{U}_{j+1}^W) - \mathbf{F}(\mathbf{U}_j^E)\}}{a_{j+\frac{1}{2}}^+ - a_{j+\frac{1}{2}}^-}, \quad (2.4)$$

and the minmod function, defined by

$$\text{minmod}(z_1, z_2, \dots) := \begin{cases} \min_k \{z_k\}, & \text{if } z_k > 0 \ \forall k, \\ \max_k \{z_k\}, & \text{if } z_k < 0 \ \forall k, \\ 0, & \text{otherwise,} \end{cases} \quad (2.5)$$

is applied both here and in (2.7), (3.4) and (3.6) below in a componentwise manner.

In (2.2)–(2.4), \mathbf{U}_j^E and \mathbf{U}_{j+1}^W stand for the respective point values of the piecewise linear reconstruction. In every cell, these values are given by

$$\mathbf{U}_j^E = \bar{\mathbf{U}}_j + \frac{\Delta x}{2} (\mathbf{U}_x)_j, \quad \mathbf{U}_{j+1}^W = \bar{\mathbf{U}}_{j+1} - \frac{\Delta x}{2} (\mathbf{U}_x)_{j+1}, \quad (2.6)$$

where the slopes $(\mathbf{U}_x)_j$ are to be computed using a nonlinear limiter to suppress oscillations. One can use, for instance, the generalized minmod limiter (see, e.g., [29,32,39,40]):

$$(\mathbf{U}_x)_j = \text{minmod}\left(\theta \frac{\bar{\mathbf{U}}_j - \bar{\mathbf{U}}_{j-1}}{\Delta x}, \frac{\bar{\mathbf{U}}_{j+1} - \bar{\mathbf{U}}_{j-1}}{2\Delta x}, \theta \frac{\bar{\mathbf{U}}_{j+1} - \bar{\mathbf{U}}_j}{\Delta x}\right), \quad (2.7)$$

where $\theta \in [1, 2]$ is a tuning parameter which helps to control the sharpness of the resulting reconstruction. A use of larger θ typically leads to less diffusive but (slightly) more oscillatory scheme.

Finally, $a_{j+\frac{1}{2}}^\pm$ are the one-sided local propagation speeds, which can be estimated, for example, by

$$\begin{aligned} a_{j+\frac{1}{2}}^+ &= \max \left\{ \lambda_N \left(\frac{\partial \mathbf{F}}{\partial \mathbf{U}} (\mathbf{U}_{j+1}^W) \right), \lambda_N \left(\frac{\partial \mathbf{F}}{\partial \mathbf{U}} (\mathbf{U}_j^E) \right), 0 \right\}, \\ a_{j+\frac{1}{2}}^- &= \min \left\{ \lambda_1 \left(\frac{\partial \mathbf{F}}{\partial \mathbf{U}} (\mathbf{U}_{j+1}^W) \right), \lambda_1 \left(\frac{\partial \mathbf{F}}{\partial \mathbf{U}} (\mathbf{U}_j^E) \right), 0 \right\}. \end{aligned} \quad (2.8)$$

Here, $\lambda_1 \leq \lambda_2 \leq \dots \leq \lambda_N$ are the N eigenvalues of the flux Jacobian $\frac{\partial \mathbf{F}}{\partial \mathbf{U}}$.

Remark 2.1. We would like to point out that the upper/lower bounds on the local speeds of propagation given in (2.8) may be inaccurate; see, for instance, [11]. However, in the numerical results reported in §4, we have used the straightforward estimates (2.8), and this did not lead to any numerical instabilities.

2.2. A sharper estimate on one-sided local speeds of propagation

In this section, we derive a new CURH scheme. Recall that in (2.8), the one-sided local propagation speeds ($a_{j+\frac{1}{2}}^\pm$) are estimated using the largest and smallest eigenvalues of the Jacobian, which makes CU schemes quite robust. These estimates, however, are not sharp and can be significantly improved especially in the cases when the data at $x = x_{j+\frac{1}{2}}$ correspond to an isolated discontinuity. In the later case, the speeds can be accurately measured using the R-H conditions, which read as

$$\Delta \mathbf{F}_{j+\frac{1}{2}} = s_{j+\frac{1}{2}} \Delta \mathbf{U}_{j+\frac{1}{2}}, \quad (2.9)$$

where $\Delta \mathbf{F}_{j+\frac{1}{2}} := \mathbf{F}(\mathbf{U}_{j+\frac{1}{2}}^+) - \mathbf{F}(\mathbf{U}_{j+\frac{1}{2}}^-)$ and $\Delta \mathbf{U}_{j+\frac{1}{2}} := \mathbf{U}_{j+\frac{1}{2}}^+ - \mathbf{U}_{j+\frac{1}{2}}^-$. However, (2.9) is not true for general data. We therefore define the following quantities:

$$s_{j+\frac{1}{2}}^{(i)} := \frac{\Delta F_{j+\frac{1}{2}}^{(i)}}{\Delta U_{j+\frac{1}{2}}^{(i)}}, \quad i = 1, \dots, N. \quad (2.10)$$

Here, we use a component notation $\Delta \mathbf{U}_{j+\frac{1}{2}} = (\Delta U_{j+\frac{1}{2}}^{(1)}, \dots, \Delta U_{j+\frac{1}{2}}^{(N)})^\top$ and likewise for other vector quantities. We note that $\Delta U_{j+\frac{1}{2}}^{(i)}$ can be equal to zero and we thus desingularize (2.10) by introducing

$$\hat{s}_{j+\frac{1}{2}}^{(i)} = \frac{2 \Delta F_{j+\frac{1}{2}}^{(i)}}{\Delta U_{j+\frac{1}{2}}^{(i)} + \Delta U_{j+\frac{1}{2}}^{(i),\varepsilon}},$$

where

$$\Delta U_{j+\frac{1}{2}}^{(i),\varepsilon} = \begin{cases} \max \left\{ \Delta U_{j+\frac{1}{2}}^{(i)}, \varepsilon \right\}, & \text{if } \Delta U_{j+\frac{1}{2}}^{(i)} > 0, \\ \min \left\{ \Delta U_{j+\frac{1}{2}}^{(i)}, -\varepsilon \right\}, & \text{otherwise.} \end{cases}$$

In the numerical examples presented in §4, we have used $\varepsilon = 10^{-10}$. In order to estimate the local speeds of propagation, we introduce the largest and the smallest R-H quantities:

$$s_{j+\frac{1}{2}}^{\max} = \max_{1 \leq i \leq N} \left\{ \hat{s}_{j+\frac{1}{2}}^{(i)} \right\} \quad \text{and} \quad s_{j+\frac{1}{2}}^{\min} = \min_{1 \leq i \leq N} \left\{ \hat{s}_{j+\frac{1}{2}}^{(i)} \right\}.$$

We then improve the estimate (2.8) according to the following algorithm.

Algorithm 2.1.

Step 1. Compute $a_{j+\frac{1}{2}}^{\pm}$ using (2.8).

Step 2. If $s_{j+\frac{1}{2}}^{\max} > \varepsilon$, then set

$$a_{j+\frac{1}{2}}^+ = \min \left\{ a_{j+\frac{1}{2}}^+, s_{j+\frac{1}{2}}^{\max} \right\} \quad \text{and} \quad a_{j+\frac{1}{2}}^- = \max \left\{ a_{j+\frac{1}{2}}^-, -s_{j+\frac{1}{2}}^{\max} \right\}.$$

Step 3. If $s_{j+\frac{1}{2}}^{\min} < -\varepsilon$, then set

$$a_{j+\frac{1}{2}}^+ = \min \left\{ a_{j+\frac{1}{2}}^+, -s_{j+\frac{1}{2}}^{\min} \right\} \quad \text{and} \quad a_{j+\frac{1}{2}}^- = \max \left\{ a_{j+\frac{1}{2}}^-, s_{j+\frac{1}{2}}^{\min} \right\}.$$

Remark 2.2. The semi-discrete CURH scheme results in a system of time-dependent ODEs (2.1), which should be integrated by a sufficiently accurate, efficient, and stable ODE solver. In the numerical experiments reported in §4, the three stage third-order strong stability preserving (SSP) Runge-Kutta method (see, e.g., [9,10]) has been used together with an adaptive time step, which is computed at every time level as follows:

$$\Delta t \leq \frac{\Delta x}{2a_{\max}}, \quad a_{\max} := \max_j \left[\max \left\{ a_{j+\frac{1}{2}}^+, -a_{j+\frac{1}{2}}^- \right\} \right].$$

3. Two-dimensional central-upwind Rankine-Hugoniot (CURH) scheme

In the 2-D case, we take the CU scheme from [17] and then improve it by obtaining sharper estimates on the one-sided local speeds of propagation.

We first introduce 2-D hyperbolic systems of conservation laws written as

$$\mathbf{U}_t + \mathbf{F}(\mathbf{U})_x + \mathbf{G}(\mathbf{U})_y = \mathbf{0}, \tag{3.1}$$

where x and y are spatial variables, t is time, $\mathbf{U}(x, y, t) \in \mathbb{R}^N$ is the vector of unknown quantities, and \mathbf{F} and \mathbf{G} are the x - and y -fluxes, respectively. We first divide the computational domain into a set of uniform Cartesian cells $C_{j,k} := [x_{j-\frac{1}{2}}, x_{j+\frac{1}{2}}] \times [y_{k-\frac{1}{2}}, y_{k+\frac{1}{2}}]$ with $x_{j+\frac{1}{2}} - x_{j-\frac{1}{2}} \equiv \Delta x$ and $y_{k+\frac{1}{2}} - y_{k-\frac{1}{2}} \equiv \Delta y$ for all j, k . As in all finite-volume methods, the computed solution is realized in terms of its cell averages $\bar{\mathbf{U}}_{j,k} \approx \frac{1}{\Delta x \Delta y} \iint_{C_{j,k}} \mathbf{U}(x, y, t) dx dy$. They are assumed to be known at a given time t , and are then evolved in time according to the following semi-discretization:

$$\frac{d}{dt} \bar{\mathbf{U}}_{j,k} = -\frac{\mathcal{F}_{j+\frac{1}{2},k} - \mathcal{F}_{j-\frac{1}{2},k}}{\Delta x} - \frac{\mathcal{G}_{j,k+\frac{1}{2}} - \mathcal{G}_{j,k-\frac{1}{2}}}{\Delta y}. \tag{3.2}$$

Here, $\mathcal{F}_{j+\frac{1}{2},k}$ and $\mathcal{G}_{j,k+\frac{1}{2}}$ are the CU numerical fluxes taken from [17]:

$$\begin{aligned} \mathcal{F}_{j+\frac{1}{2},k} &= \frac{a_{j+\frac{1}{2},k}^+ \mathbf{F}(\mathbf{U}_{j,k}^E) - a_{j+\frac{1}{2},k}^- \mathbf{F}(\mathbf{U}_{j+1,k}^W)}{a_{j+\frac{1}{2},k}^+ - a_{j+\frac{1}{2},k}^-} + \frac{a_{j+\frac{1}{2},k}^+ a_{j+\frac{1}{2},k}^-}{a_{j+\frac{1}{2},k}^+ - a_{j+\frac{1}{2},k}^-} \left[\mathbf{U}_{j+1,k}^W - \mathbf{U}_{j,k}^E - \delta \mathbf{U}_{j+\frac{1}{2},k} \right], \\ \mathcal{G}_{j,k+\frac{1}{2}} &= \frac{b_{j,k+\frac{1}{2}}^+ \mathbf{G}(\mathbf{U}_{j,k}^N) - b_{j,k+\frac{1}{2}}^- \mathbf{G}(\mathbf{U}_{j,k+1}^S)}{b_{j,k+\frac{1}{2}}^+ - b_{j,k+\frac{1}{2}}^-} + \frac{b_{j,k+\frac{1}{2}}^+ b_{j,k+\frac{1}{2}}^-}{b_{j,k+\frac{1}{2}}^+ - b_{j,k+\frac{1}{2}}^-} \left[\mathbf{U}_{j,k+1}^S - \mathbf{U}_{j,k}^N - \delta \mathbf{U}_{j,k+\frac{1}{2}} \right]. \end{aligned} \tag{3.3}$$

The built-in “anti-diffusion” terms $\delta\mathbf{U}_{j+\frac{1}{2},k}$ and $\delta\mathbf{U}_{j,k+\frac{1}{2}}$ are given by

$$\begin{aligned}\delta\mathbf{U}_{j+\frac{1}{2},k} &= \text{minmod}\left(\mathbf{U}_{j+1,k}^{\text{SW}} - \mathbf{U}_{j+\frac{1}{2},k}^*, \mathbf{U}_{j+\frac{1}{2},k}^* - \mathbf{U}_{j,k}^{\text{SE}}, \mathbf{U}_{j+1,k}^{\text{NW}} - \mathbf{U}_{j+\frac{1}{2},k}^*, \mathbf{U}_{j+\frac{1}{2},k}^* - \mathbf{U}_{j,k}^{\text{NE}}\right), \\ \delta\mathbf{U}_{j,k+\frac{1}{2}} &= \text{minmod}\left(\mathbf{U}_{j,k+1}^{\text{SW}} - \mathbf{U}_{j,k+\frac{1}{2}}^*, \mathbf{U}_{j,k+\frac{1}{2}}^* - \mathbf{U}_{j,k}^{\text{NW}}, \mathbf{U}_{j,k+1}^{\text{SE}} - \mathbf{U}_{j,k+\frac{1}{2}}^*, \mathbf{U}_{j,k+\frac{1}{2}}^* - \mathbf{U}_{j,k}^{\text{NE}}\right),\end{aligned}\quad (3.4)$$

where

$$\begin{aligned}\mathbf{U}_{j+\frac{1}{2},k}^* &= \frac{a_{j+\frac{1}{2},k}^+ \mathbf{U}_{j+1,k}^{\text{W}} - a_{j+\frac{1}{2},k}^- \mathbf{U}_{j,k}^{\text{E}} - \left\{ \mathbf{F}(\mathbf{U}_{j+1,k}^{\text{W}}) - \mathbf{F}(\mathbf{U}_{j,k}^{\text{E}}) \right\}}{a_{j+\frac{1}{2},k}^+ - a_{j+\frac{1}{2},k}^-}, \\ \mathbf{U}_{j,k+\frac{1}{2}}^* &= \frac{b_{j,k+\frac{1}{2}}^+ \mathbf{U}_{j,k+1}^{\text{S}} - b_{j,k+\frac{1}{2}}^- \mathbf{U}_{j,k}^{\text{N}} - \left\{ \mathbf{G}(\mathbf{U}_{j,k+1}^{\text{S}}) - \mathbf{G}(\mathbf{U}_{j,k}^{\text{N}}) \right\}}{b_{j,k+\frac{1}{2}}^+ - b_{j,k+\frac{1}{2}}^-}.\end{aligned}\quad (3.5)$$

In (3.2)–(3.5), the corresponding point values of \mathbf{U} are

$$\begin{aligned}\mathbf{U}_{j,k}^{\text{E}} &= \bar{\mathbf{U}}_{j,k} + \frac{\Delta x}{2} (\mathbf{U}_x)_{j,k}, & \mathbf{U}_{j,k}^{\text{W}} &= \bar{\mathbf{U}}_{j,k} - \frac{\Delta x}{2} (\mathbf{U}_x)_{j,k}, \\ \mathbf{U}_{j,k}^{\text{N}} &= \bar{\mathbf{U}}_{j,k} + \frac{\Delta y}{2} (\mathbf{U}_y)_{j,k}, & \mathbf{U}_{j,k}^{\text{S}} &= \bar{\mathbf{U}}_{j,k} - \frac{\Delta y}{2} (\mathbf{U}_y)_{j,k}, \\ \mathbf{U}_{j,k}^{\text{NE}} &= \bar{\mathbf{U}}_{j,k} + \frac{\Delta x}{2} (\mathbf{U}_x)_{j,k} + \frac{\Delta y}{2} (\mathbf{U}_y)_{j,k}, & \mathbf{U}_{j,k}^{\text{NW}} &= \bar{\mathbf{U}}_{j,k} - \frac{\Delta x}{2} (\mathbf{U}_x)_{j,k} + \frac{\Delta y}{2} (\mathbf{U}_y)_{j,k}, \\ \mathbf{U}_{j,k}^{\text{SE}} &= \bar{\mathbf{U}}_{j,k} + \frac{\Delta x}{2} (\mathbf{U}_x)_{j,k} - \frac{\Delta y}{2} (\mathbf{U}_y)_{j,k}, & \mathbf{U}_{j,k}^{\text{SW}} &= \bar{\mathbf{U}}_{j,k} - \frac{\Delta x}{2} (\mathbf{U}_x)_{j,k} - \frac{\Delta y}{2} (\mathbf{U}_y)_{j,k}.\end{aligned}$$

The slopes $(\mathbf{U}_x)_{j,k}$ and $(\mathbf{U}_y)_{j,k}$ are to be computed using a nonlinear limiter to reduce spurious oscillations. As in the 1-D case, we have used the generalized minmod limiter:

$$\begin{aligned}(\mathbf{U}_x)_{j,k} &= \text{minmod}\left(\theta \frac{\bar{\mathbf{U}}_{j,k} - \bar{\mathbf{U}}_{j-1,k}}{\Delta x}, \frac{\bar{\mathbf{U}}_{j+1,k} - \bar{\mathbf{U}}_{j-1,k}}{2\Delta x}, \theta \frac{\bar{\mathbf{U}}_{j+1,k} - \bar{\mathbf{U}}_{j,k}}{\Delta x}\right), \\ (\mathbf{U}_y)_{j,k} &= \text{minmod}\left(\theta \frac{\bar{\mathbf{U}}_{j,k} - \bar{\mathbf{U}}_{j,k-1}}{\Delta y}, \frac{\bar{\mathbf{U}}_{j,k+1} - \bar{\mathbf{U}}_{j,k-1}}{2\Delta y}, \theta \frac{\bar{\mathbf{U}}_{j,k+1} - \bar{\mathbf{U}}_{j,k}}{\Delta y}\right),\end{aligned}\quad \theta \in [1, 2].\quad (3.6)$$

Finally, $a_{j+\frac{1}{2},k}^\pm$ and $b_{j,k+\frac{1}{2}}^\pm$ are the one-sided local speeds of propagations in x - and y -directions respectively. In [17], they were estimated by

$$\begin{aligned}a_{j+\frac{1}{2},k}^+ &= \max\left\{\lambda_N\left(\frac{\partial \mathbf{F}}{\partial \mathbf{U}}(\mathbf{U}_{j+1,k}^{\text{W}})\right), \lambda_N\left(\frac{\partial \mathbf{F}}{\partial \mathbf{U}}(\mathbf{U}_{j,k}^{\text{E}})\right), 0\right\}, \\ a_{j+\frac{1}{2},k}^- &= \min\left\{\lambda_1\left(\frac{\partial \mathbf{F}}{\partial \mathbf{U}}(\mathbf{U}_{j+1,k}^{\text{W}})\right), \lambda_1\left(\frac{\partial \mathbf{F}}{\partial \mathbf{U}}(\mathbf{U}_{j,k}^{\text{E}})\right), 0\right\}, \\ b_{j,k+\frac{1}{2}}^+ &= \max\left\{\lambda_N\left(\frac{\partial \mathbf{G}}{\partial \mathbf{U}}(\mathbf{U}_{j,k+1}^{\text{S}})\right), \lambda_N\left(\frac{\partial \mathbf{G}}{\partial \mathbf{U}}(\mathbf{U}_{j,k}^{\text{N}})\right), 0\right\}, \\ b_{j,k+\frac{1}{2}}^- &= \min\left\{\lambda_1\left(\frac{\partial \mathbf{G}}{\partial \mathbf{U}}(\mathbf{U}_{j,k+1}^{\text{S}})\right), \lambda_1\left(\frac{\partial \mathbf{G}}{\partial \mathbf{U}}(\mathbf{U}_{j,k}^{\text{N}})\right), 0\right\}.\end{aligned}\quad (3.7)$$

Here, $\lambda_1 \leq \dots \leq \lambda_N$ are the N eigenvalues of the corresponding Jacobians $\frac{\partial \mathbf{F}}{\partial \mathbf{U}}$ and $\frac{\partial \mathbf{G}}{\partial \mathbf{U}}$.

3.1. Numerical dissipation switch mechanism

In the recent papers [18,19], the amount of numerical dissipation present in 2-D CU schemes was locally reduced by using the numerical dissipation switch mechanism. The switch applies in the areas of contact lines and shear layers. We will briefly describe the switch for the Euler equations of gas dynamics which was developed in [18]. The 2-D Euler equations of gas dynamics read as

$$\begin{aligned} \rho_t + (\rho u)_x + (\rho v)_y &= 0, \\ (\rho u)_t + (\rho u^2 + p)_x + (\rho uv)_y &= 0, \\ (\rho v)_t + (\rho uv)_x + (\rho v^2 + p)_y &= 0, \\ E_t + [u(E + p)]_x + [v(E + p)]_y &= 0. \end{aligned} \tag{3.8}$$

Here, ρ is the density, u and v are the x - and y -velocities, p is the pressure, and E is the total energy which, in the case of ideal gas, is related to the other thermodynamical quantities through the following equation of states:

$$E = \frac{p}{\gamma - 1} + \frac{\rho}{2} (u^2 + v^2),$$

where γ is the specific heat ratio.

Notice that for the system (3.8), the equations in (3.7) read as

$$\begin{aligned} a_{j+\frac{1}{2},k}^+ &= \max \left\{ u_{j,k}^E + c_{j,k}^E, u_{j+1,k}^W + c_{j+1,k}^W, 0 \right\}, \\ a_{j+\frac{1}{2},k}^- &= \min \left\{ u_{j,k}^E - c_{j,k}^E, u_{j+1,k}^W - c_{j+1,k}^W, 0 \right\}, \\ b_{j,k+\frac{1}{2}}^+ &= \max \left\{ v_{j,k}^N + c_{j,k}^N, v_{j,k+1}^S + c_{j,k+1}^S, 0 \right\}, \\ b_{j,k+\frac{1}{2}}^- &= \min \left\{ v_{j,k}^N - c_{j,k}^N, v_{j,k+1}^S - c_{j,k+1}^S, 0 \right\}, \end{aligned} \tag{3.9}$$

where $c := \sqrt{\gamma p / \rho}$ is the speed of sound, and

$$\begin{aligned} u_{j,k}^E &= \frac{(\bar{\rho}u)_{j,k}^E}{\bar{\rho}_{j,k}^E}, \quad u_{j+1,k}^W = \frac{(\bar{\rho}u)_{j+1,k}^W}{\bar{\rho}_{j+1,k}^W}, \quad u_{j,k}^N = \frac{(\bar{\rho}u)_{j,k}^N}{\bar{\rho}_{j,k}^N}, \quad u_{j,k+1}^S = \frac{(\bar{\rho}u)_{j,k+1}^S}{\bar{\rho}_{j,k+1}^S}, \\ v_{j,k}^E &= \frac{(\bar{\rho}v)_{j,k}^E}{\bar{\rho}_{j,k}^E}, \quad v_{j+1,k}^W = \frac{(\bar{\rho}v)_{j+1,k}^W}{\bar{\rho}_{j+1,k}^W}, \quad v_{j,k}^N = \frac{(\bar{\rho}v)_{j,k}^N}{\bar{\rho}_{j,k}^N}, \quad v_{j,k+1}^S = \frac{(\bar{\rho}v)_{j,k+1}^S}{\bar{\rho}_{j,k+1}^S}, \\ p_{j,k}^E &= (\gamma - 1) \left[\bar{E}_{j,k}^E - \frac{\bar{\rho}_{j,k}^E}{2} \left((u_{j,k}^E)^2 + (v_{j,k}^E)^2 \right) \right], \\ p_{j+1,k}^W &= (\gamma - 1) \left[\bar{E}_{j+1,k}^W - \frac{\bar{\rho}_{j+1,k}^W}{2} \left((u_{j+1,k}^W)^2 + (v_{j+1,k}^W)^2 \right) \right], \\ p_{j,k}^N &= (\gamma - 1) \left[\bar{E}_{j,k}^N - \frac{\bar{\rho}_{j,k}^N}{2} \left((u_{j,k}^N)^2 + (v_{j,k}^N)^2 \right) \right], \\ p_{j,k+1}^S &= (\gamma - 1) \left[\bar{E}_{j,k+1}^S - \frac{\bar{\rho}_{j,k+1}^S}{2} \left((u_{j,k+1}^S)^2 + (v_{j,k+1}^S)^2 \right) \right], \\ c_{j,k}^E &= \sqrt{\frac{\gamma p_{j,k}^E}{\bar{\rho}_{j,k}^E}}, \quad c_{j+1,k}^W = \sqrt{\frac{\gamma p_{j+1,k}^W}{\bar{\rho}_{j+1,k}^W}}, \quad c_{j,k}^N = \sqrt{\frac{\gamma p_{j,k}^N}{\bar{\rho}_{j,k}^N}}, \quad c_{j,k+1}^S = \sqrt{\frac{\gamma p_{j,k+1}^S}{\bar{\rho}_{j,k+1}^S}}. \end{aligned}$$

The main idea of the numerical dissipation switch is to reduce the local propagation speeds in the areas where the solution is near/at contact waves and shear layers. To this end, we replace (3.9) with the following modified local propagation speeds:

$$\begin{aligned} a_{j+\frac{1}{2},k}^+ &= \max \left\{ u_{j,k}^E + \alpha_{j+\frac{1}{2},k} c_{j,k}^E, u_{j+1,k}^W + \alpha_{j+\frac{1}{2},k} c_{j+1,k}^W, 0 \right\}, \\ a_{j+\frac{1}{2},k}^- &= \min \left\{ u_{j,k}^E - \alpha_{j+\frac{1}{2},k} c_{j,k}^E, u_{j+1,k}^W - \alpha_{j+\frac{1}{2},k} c_{j+1,k}^W, 0 \right\}, \\ b_{j,k+\frac{1}{2}}^+ &= \max \left\{ v_{j,k}^N + \beta_{j,k+\frac{1}{2}} c_{j,k}^N, v_{j,k+1}^S + \beta_{j,k+\frac{1}{2}} c_{j,k+1}^S, 0 \right\}, \\ b_{j,k+\frac{1}{2}}^- &= \min \left\{ v_{j,k}^N - \beta_{j,k+\frac{1}{2}} c_{j,k}^N, v_{j,k+1}^S - \beta_{j,k+\frac{1}{2}} c_{j,k+1}^S, 0 \right\}, \end{aligned} \tag{3.10}$$

where both $\alpha_{j+\frac{1}{2},k}$ and $\beta_{j,k+\frac{1}{2}}$ are given by (see [18])

$$\alpha_{j+\frac{1}{2},k} = \begin{cases} \frac{\Delta\alpha_{j+\frac{1}{2},k}^{(1)}}{\Delta\alpha_{j+\frac{1}{2},k}}, & \text{if } \Delta\alpha_{j+\frac{1}{2},k} > \varepsilon, \\ 0, & \text{otherwise,} \end{cases}$$

where

$$\Delta\alpha_{j+\frac{1}{2},k}^{(1)} = \left| \frac{p_{j+1,k}^W - p_{j,k}^E}{\gamma - 1} + \frac{\rho_{j+1,k}^W (u_{j+1,k}^W)^2 - \rho_{j,k}^E (u_{j,k}^E)^2}{2} \right|,$$

$$\Delta\alpha_{j+\frac{1}{2},k}^{(2)} = \left| \frac{\rho_{j+1,k}^W (v_{j+1,k}^W)^2 - \rho_{j,k}^E (v_{j,k}^E)^2}{2} \right|, \quad \Delta\alpha_{j+\frac{1}{2},k} = \sqrt{\left(\Delta\alpha_{j+\frac{1}{2},k}^{(1)} \right)^2 + \left(\Delta\alpha_{j+\frac{1}{2},k}^{(2)} \right)^2},$$

and

$$\beta_{j,k+\frac{1}{2}} = \begin{cases} \frac{\Delta\beta_{j,k+\frac{1}{2}}^{(1)}}{\Delta\beta_{j,k+\frac{1}{2}}}, & \text{if } \Delta\beta_{j,k+\frac{1}{2}} > \varepsilon, \\ 0, & \text{otherwise,} \end{cases}$$

where

$$\Delta\beta_{j,k+\frac{1}{2}}^{(1)} = \left| \frac{p_{j,k+1}^S - p_{j,k}^N}{\gamma - 1} + \frac{\rho_{j,k+1}^S (v_{j,k+1}^S)^2 - \rho_{j,k}^N (v_{j,k}^N)^2}{2} \right|,$$

$$\Delta\beta_{j,k+\frac{1}{2}}^{(2)} = \left| \frac{\rho_{j,k+1}^S (u_{j,k+1}^S)^2 - \rho_{j,k}^N (u_{j,k}^N)^2}{2} \right|, \quad \Delta\beta_{j,k+\frac{1}{2}} = \sqrt{\left(\Delta\beta_{j,k+\frac{1}{2}}^{(1)} \right)^2 + \left(\Delta\beta_{j,k+\frac{1}{2}}^{(2)} \right)^2},$$

respectively. Here, ε is a small positive number needed to avoid division by zero. We have taken $\varepsilon = 10^{-10}$ in the numerical examples reported in §4.

3.2. A sharper estimate on one-sided local speeds of propagation

We now follow the 1-D R-H approach developed in §2.2 and apply it to $a_{j+\frac{1}{2},k}^\pm$ and $b_{j,k+\frac{1}{2}}^\pm$ given by (3.10). We begin with the x -directional flux \mathbf{F} and introduce

$$\hat{s}_{j+\frac{1}{2},k}^{(i)} = \frac{2\Delta F_{j+\frac{1}{2},k}^{(i)}}{\Delta U_{j+\frac{1}{2},k}^{(i)} + \Delta U_{j+\frac{1}{2},k}^{(i),\varepsilon}}, \quad i = 1, \dots, N,$$

where

$$\Delta U_{j+\frac{1}{2},k}^{(i),\varepsilon} = \begin{cases} \max \left\{ \Delta U_{j+\frac{1}{2},k}^{(i)}, \varepsilon \right\}, & \text{if } \Delta U_{j+\frac{1}{2},k}^{(i)} > 0, \\ \min \left\{ \Delta U_{j+\frac{1}{2},k}^{(i)}, -\varepsilon \right\}, & \text{otherwise.} \end{cases}$$

Then, the largest and the smallest local R-H quantities are

$$s_{j+\frac{1}{2},k}^{\max} = \max_{1 \leq i \leq N} \left\{ \hat{s}_{j+\frac{1}{2},k}^{(i)} \right\} \quad \text{and} \quad s_{j+\frac{1}{2},k}^{\min} = \min_{1 \leq i \leq N} \left\{ \hat{s}_{j+\frac{1}{2},k}^{(i)} \right\}.$$

Finally, the improved estimates of the x -directional one-sided local propagation speeds are obtained according to the following algorithm.

Algorithm 3.1.

Step 1. Compute $a_{j+\frac{1}{2},k}^\pm$ using (3.10).

Step 2. If $s_{j+\frac{1}{2},k}^{\max} > \varepsilon$, then set

$$a_{j+\frac{1}{2},k}^+ = \min \left\{ a_{j+\frac{1}{2},k}^+, s_{j+\frac{1}{2},k}^{\max} \right\} \quad \text{and} \quad a_{j+\frac{1}{2},k}^- = \max \left\{ a_{j+\frac{1}{2},k}^-, -s_{j+\frac{1}{2},k}^{\max} \right\}.$$

Step 3. If $s_{j+\frac{1}{2},k}^{\min} < -\varepsilon$, then set

$$a_{j+\frac{1}{2},k}^+ = \min \left\{ a_{j+\frac{1}{2},k}^+, -s_{j+\frac{1}{2},k}^{\min} \right\} \quad \text{and} \quad a_{j+\frac{1}{2},k}^- = \max \left\{ a_{j+\frac{1}{2},k}^-, s_{j+\frac{1}{2},k}^{\min} \right\}.$$

Remark 3.1. We have applied the above approach to improve the estimate (3.10) on the one-sided local speeds of propagation. It can be applied to the original estimate (3.7) (or (3.9) in the case of the 2-D Euler equations of gas dynamics) as well.

An improved estimate of the y -directional one-sided local speeds of propagation ($b_{j,k+\frac{1}{2}}^{\pm}$) can be obtained in a similar manner.

Remark 3.2. As in the 1-D case, the 2-D semi-discrete CURH scheme results in a system of time-dependent ODEs (3.2), which we have integrated using the same three stage third-order SSP Runge-Kutta method. The time steps have been selected adaptively using the following CFL-type condition:

$$\Delta t \leq \frac{1}{2} \min \left\{ \frac{\Delta x}{a_{\max}}, \frac{\Delta y}{b_{\max}} \right\},$$

where

$$a_{\max} := \max_{j,k} \left[\max \left\{ a_{j+\frac{1}{2},k}^+, -a_{j+\frac{1}{2},k}^- \right\} \right], \quad b_{\max} := \max_{j,k} \left[\max \left\{ b_{j,k+\frac{1}{2}}^+, -b_{j,k+\frac{1}{2}}^- \right\} \right].$$

4. Numerical examples

In this section, we present various 1-D and 2-D numerical examples. Our main objective is to demonstrate that the R-H based CU schemes developed in §2 and §3 lead to the higher resolution of contact and shock waves, shear layers, vortices as well as large-scale 2-D structures. In Examples 1–7, the ratio of specific heats is taken to be $\gamma = 1.4$, while in Example 8, we take $\gamma = 5/3$. In all of the examples, we have used the CFL number 0.45.

4.1. One-dimensional examples

We consider the 1-D Euler equations of gas dynamics:

$$\begin{aligned} \rho_t + (\rho u)_x &= 0, \\ (\rho u)_t + (\rho u^2 + p)_x &= 0, \\ E_t + [u(E + p)]_x &= 0, \end{aligned}$$

where, as in the 2-D case, ρ is the density, u is the velocity, p is the pressure, and E is the total energy, which is related to the other thermodynamical quantities through the equation of states:

$$E = \frac{p}{\gamma - 1} + \frac{\rho u^2}{2}.$$

In all of the 1-D numerical examples, we will use the Riemann initial data on the computational domain $[0, 1]$ subject to free (zero-order extrapolation) boundary conditions. We have tested the CURH scheme on a wide variety of Riemann problems, and the obtained results (most of which are not reported here for the sake of brevity) clearly indicate that the proposed CURH scheme is as robust as the original CU scheme. In Examples 1 and 2 below, we show the computations of some specific Riemann problems for which the CURH scheme exhibits improved results compared to the CU scheme.

Example 1 (Slowly moving isolated contact discontinuity). In the first example, the following initial conditions are taken:

$$(\rho(x, 0), u(x, 0), p(x, 0)) = \begin{cases} (1.4, 0.1, 1), & x < 0.3, \\ (1.0, 0.1, 1), & x > 0.3. \end{cases}$$

This example is useful for assessing the isolated contact capturing ability of numerical schemes.

We compute the CURH and CU solutions until the final time $t = 2$ on a uniform grid with $\Delta x = 1/100$. We first test the first-order versions of both schemes, which are obtained by setting $(\mathbf{U}_x)_j \equiv \mathbf{0}$ in (2.6). The obtained densities are presented in Fig. 4.1, where one can see that the first-order CURH scheme clearly outperforms the first-order CU scheme. We then test the corresponding second-order schemes and show the obtained results in Fig. 4.2. As expected, the CURH achieves a slightly better resolution of the isolated contact wave even though the difference is not as pronounced as in the first-order case.

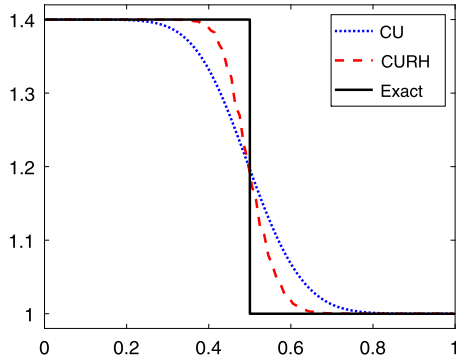


Fig. 4.1. Example 1: Density (ρ) computed using both the CURH and CU first-order schemes.

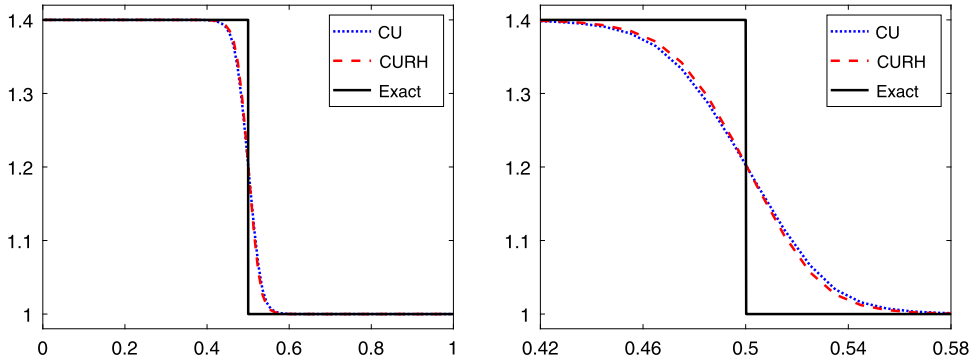


Fig. 4.2. Example 1: Density (ρ) computed by both the CURH and CU second-order schemes (left) and zoom at the contact discontinuity area (right).

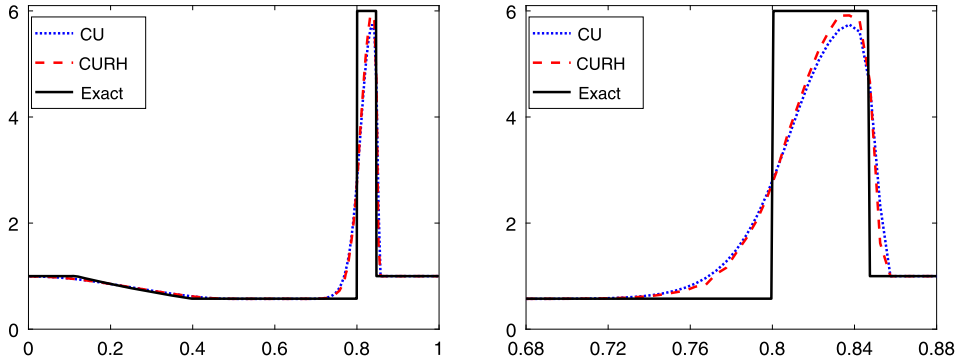


Fig. 4.3. Example 2: Density (ρ) computed by both the CURH and CU first-order schemes (left) and zoom at the contact discontinuity area (right).

Example 2 (Stationary contact wave and traveling shock and rarefaction). In this example taken from [17], the initial data are

$$(\rho(x, 0), u(x, 0), p(x, 0)) = \begin{cases} (1, -19.59745, 1000), & x < 0.8, \\ (1, -19.59745, 0.01), & x > 0.8. \end{cases}$$

The exact solution of this initial-value problem consists of a stationary contact wave, a traveling shock, and a traveling rarefaction wave. We compute the CURH and CU solutions until the final time $t = 0.012$ on a uniform grid with $\Delta x = 1/200$. As in Example 1, we first test the first-order versions of the schemes and present the obtained results in Fig. 4.3. As one can see, the first-order CURH scheme outperforms the first-order CU scheme, while the second-order CURH results are only slightly better than the second-order CU results; see in Fig. 4.4.

4.2. Two-dimensional examples

In the 2-D examples, we test the proposed CURH scheme and compare its performance with the original CU scheme, the CU scheme with the numerical dissipation switch recently proposed in [18,19], and the CURH scheme without the

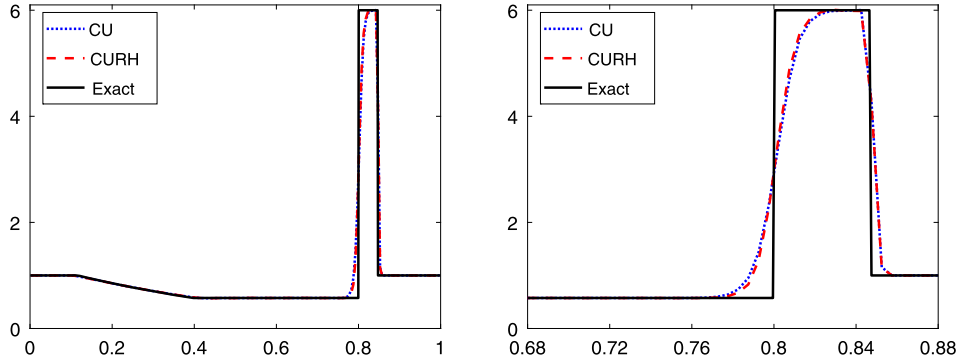


Fig. 4.4. Example 2: Density (ρ) computed by both the CURH and CU second-order schemes (left) and zoom at the contact discontinuity area (right).

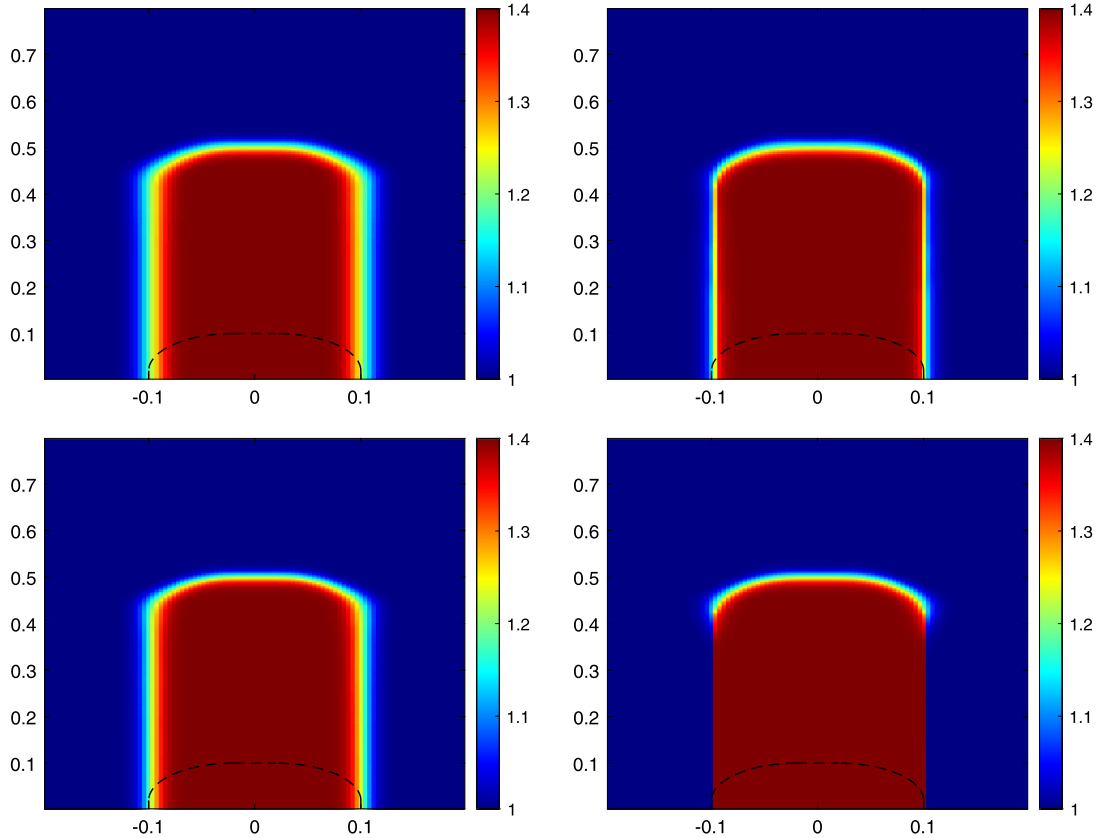


Fig. 4.5. Example 3: Density (ρ) computed by the CU (top left), Switch CU (top right), CURH-WS (bottom left) and CURH (bottom right) schemes. (For interpretation of the colors in the figure(s), the reader is referred to the web version of this article.)

numerical dissipation switch. Below, we will refer to the CU scheme with the numerical dissipation switch as to the “Switch CU scheme” and the CURH scheme without the numerical dissipation switch as the “CURH-WS scheme”. Our goal is to show that combining the two discussed numerical dissipation reduction techniques (the discrete R-H conditions and the numerical dissipation switch mechanism) lead to a more accurate, yet highly robust central-upwind scheme—the CURH scheme.

Example 3 (Moving contact waves). In the first 2-D test taken from [18], we consider an isolated moving contact wave in the computational domain $\Omega = [-0.2, 0.2] \times [0, 0.8]$ with the following initial data:

$$(\rho(x, y, 0), u(x, y, 0), v(x, y, 0), p(x, y, 0)) = \begin{cases} (1.4, 0, 0.2, 1), & (x, y) \in D, \\ (1.0, 0, 0.2, 1), & \text{otherwise.} \end{cases}$$

The domain D consists of the points $(x, y) \in \Omega$ that satisfy the following conditions:

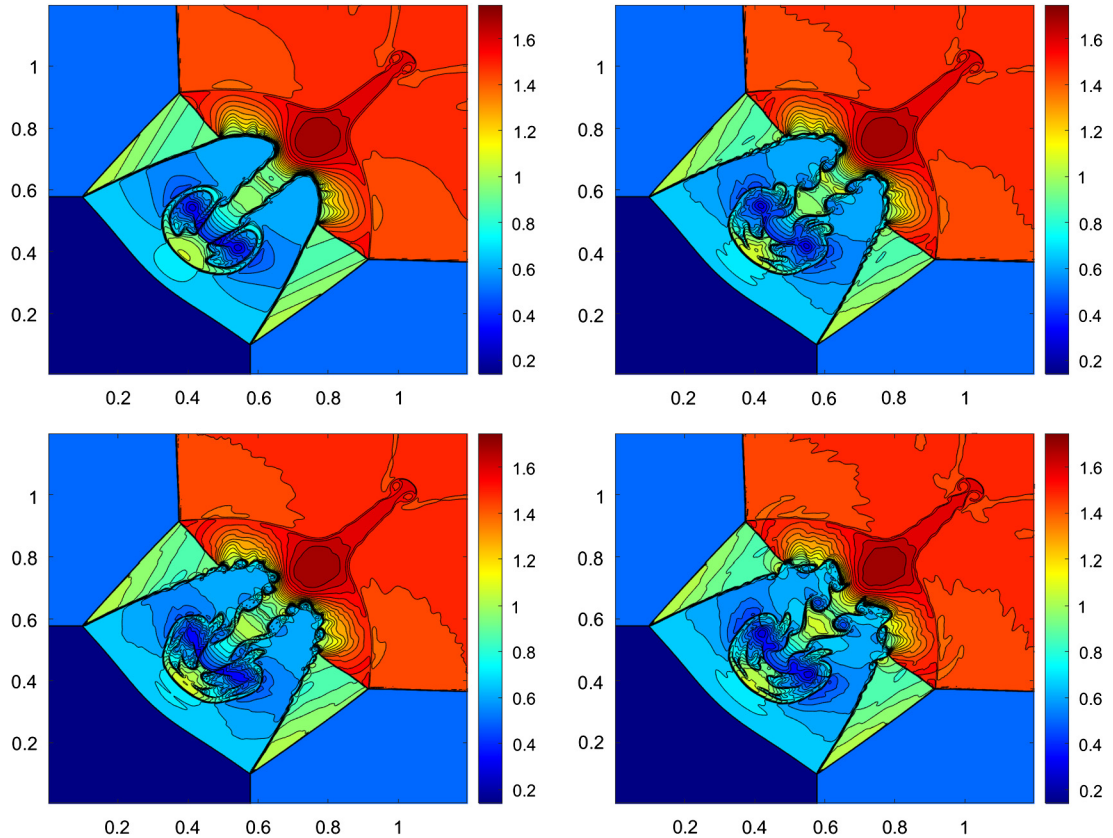


Fig. 4.6. Example 4: Density (ρ) computed by the CU (top left), Switch CU (top right), CURH-WS (bottom left) and CURH (bottom right) schemes.

$$\{-0.1 < x < 0.1, 0 < y < 0.02\} \cup \{-0.02 < x < 0.02, 0.02 < y < 0.1\} \cup \\ \{(x + 0.02)^2 + (y - 0.02)^2 < 0.08^2\} \cup \{(x - 0.02)^2 + (y - 0.02)^2 < 0.08^2\}.$$

We impose free boundary conditions and compute the solution until the final time $t = 2$ on the uniform grid with $\Delta x = \Delta y = 1/250$. The densities computed by all of the studied schemes are shown in Fig. 4.5. As one can see, the CURH-WS scheme produces slightly better resolution of contact waves in comparison with the CU scheme, and the Switch CU scheme in this case outperforms the CURH-WS scheme. As expected, the proposed CURH scheme clearly achieves the best resolution among all of the schemes.

Example 4 (Two-dimensional Riemann problem). We now consider Configuration 3 of the 2-D Riemann problems from [23]; see also [24,36,37,42]. The initial conditions are

$$(\rho(x, y, 0), u(x, y, 0), v(x, y, 0), p(x, y, 0)) = \begin{cases} (1.5, 0, 0, 1.5), & x > 1, y > 1, \\ (0.5323, 1.206, 0, 0.3), & x < 1, y > 1, \\ (0.138, 1.206, 1.206, 0.029), & x < 1, y < 1, \\ (0.5323, 0, 1.206, 0.3), & x > 1, y < 1. \end{cases}$$

The computational domain $[0, 1.2] \times [0, 1.2]$ is divided into 1000×1000 uniform cells with $\Delta x = \Delta y = 3/2500$. We impose free boundary conditions and compute the solution until the final time $t = 1$. The densities computed by all of the studied schemes are shown in Fig. 4.6. As one can see, the large-scale flow structures such as the triple point, incident shock, reflected shock, Mach stem, and slip plane are resolved in a better manner by the newly proposed CURH scheme compared with the results obtained using the CU, Switch CU, and CURH-WS schemes. Also, the instability along the jet's neck is more pronounced with a stronger vorticity deposition in the CURH solution.

Example 5 (Explosion problem). In this example, we consider the explosion problem, which is taken from [30] and also used in [17,18,21]. The initial conditions are

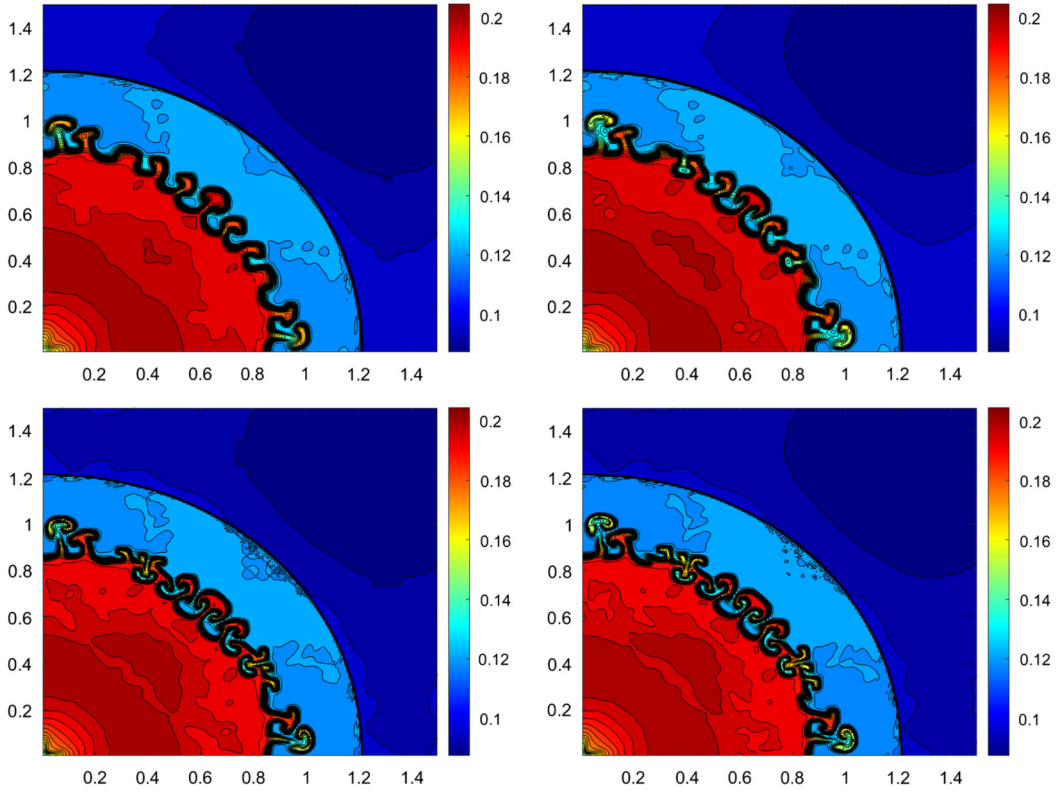


Fig. 4.7. Example 5: Density (ρ) computed by the CU (top left), Switch CU (top right), CURH-WS (bottom left) and CURH (bottom right) schemes.

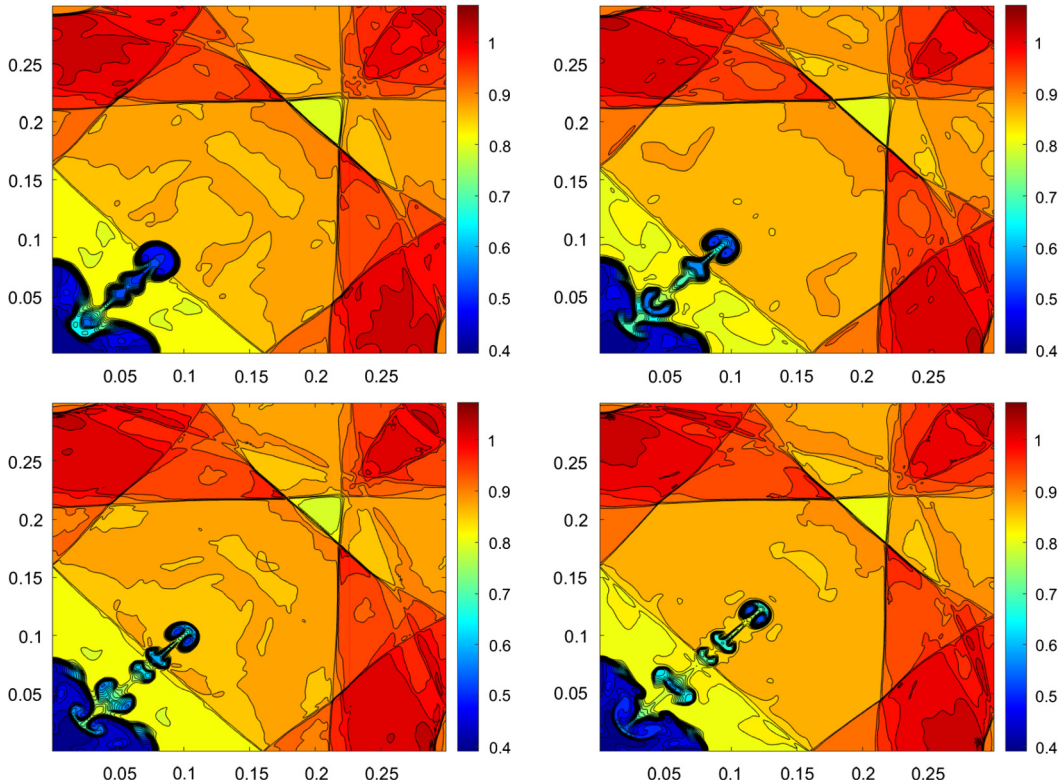


Fig. 4.8. Example 6: Density (ρ) computed by the CU (top left), Switch CU (top right), CURH-WS (bottom left) and CURH (bottom right) schemes with $\Delta x = \Delta y = 3/6000$.

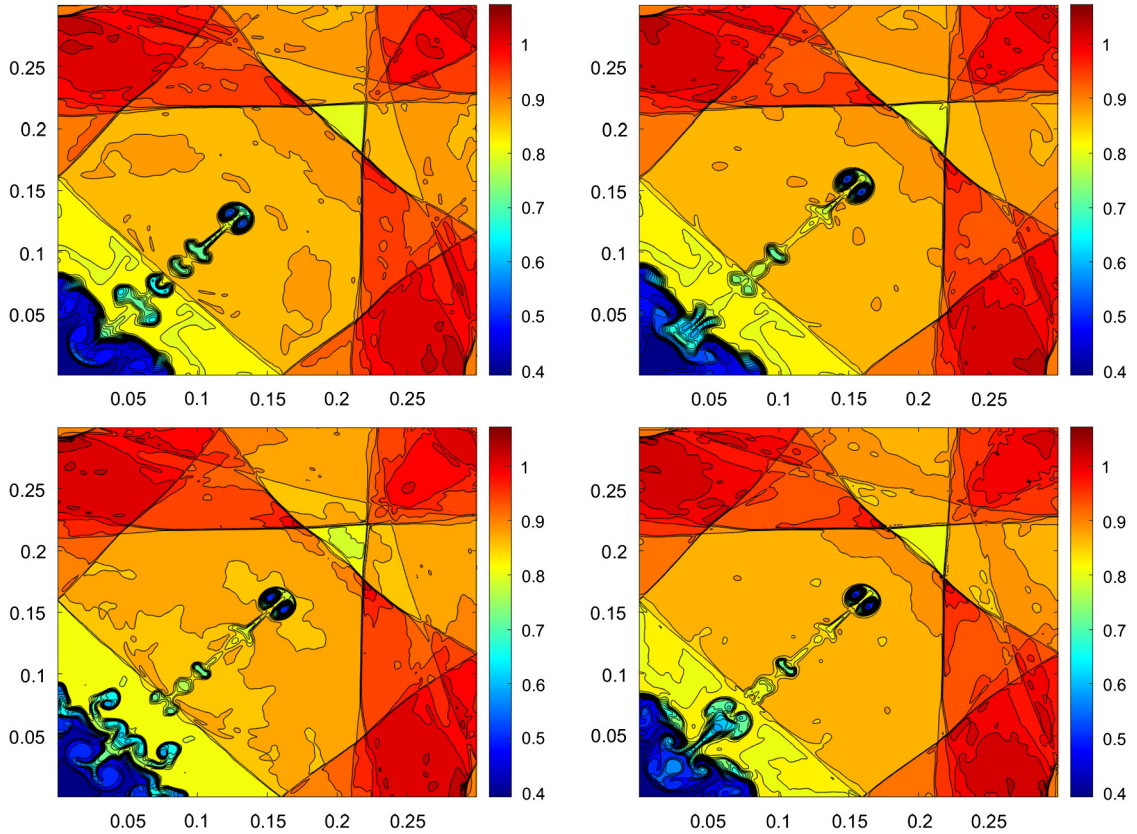


Fig. 4.9. Example 6: Density (ρ) computed by the CU (top left), Switch CU (top right), CURH-WS (bottom left) and CURH (bottom right) schemes with $\Delta x = \Delta y = 3/8000$.

$$(\rho(x, y, 0), u(x, y, 0), v(x, y, 0), p(x, y, 0)) = \begin{cases} (1, 0, 0, 1), & x^2 + y^2 < 0.16, \\ (0.125, 0, 0, 0.1), & \text{otherwise.} \end{cases}$$

We compute the solution using the uniform mesh with $\Delta x = \Delta y = 3/800$ in the computational domain $[0, 1.5] \times [0, 1.5]$. We set the reflecting (solid wall) boundary conditions at $x = 0$ and $y = 0$, and free boundary conditions at $x = 1.5$ and $y = 1.5$. The densities computed by all of the studied schemes at the final time $t = 3.2$ are plotted in Fig. 4.7. As one can clearly see, the proposed CURH-WS and CURH schemes yield much higher resolution results compared to the CU and Switch CU schemes. This is reflected in the fact that the contact curve captured by the CURH-WS and CURH schemes is much “curlier” and thus more unstable than that of the CU and Switch CU schemes. This again indicates, in particular, the low dissipation property of the CURH scheme as the contact curve is supposed to be unstable and may be stabilized by excessive numerical dissipation only.

Example 6 (Implosion problem). We then test the implosion problem, also taken from [30] and used in [17,18,21]. The initial conditions,

$$(\rho(x, y, 0), u(x, y, 0), v(x, y, 0), p(x, y, 0)) = \begin{cases} (0.125, 0, 0, 0.14), & |x| + |y| < 0.15, \\ (1, 0, 0, 1), & \text{otherwise,} \end{cases}$$

are prescribed in the computational domain $[0, 0.3] \times [0, 0.3]$ with the reflecting (solid wall) boundary conditions. In Figs. 4.8 and 4.9, we plot the ρ -component of the numerical solutions at final time $t = 2.5$ computed using the CU, Switch CU, CURH-WS, and CURH schemes respectively, using two different uniform meshes with $\Delta x = \Delta y = 3/6000$ and $3/8000$. As one can observe, all of the schemes produce more accurate results as the mesh is refined. Moreover, if we compare the differences between these schemes, we find that the jets generated by the CURH-WS and CURH schemes propagate to a larger extent than the jets produced by the CU and Switch CU schemes, respectively. Again, it is worth noting that the numerical dissipation switch mechanism plays a vital role in reducing numerical dissipation when coupled with the CURH-WS scheme. Consequently, one can conclude that the CURH scheme has a much smaller amount of numerical dissipation compared to its counterparts.

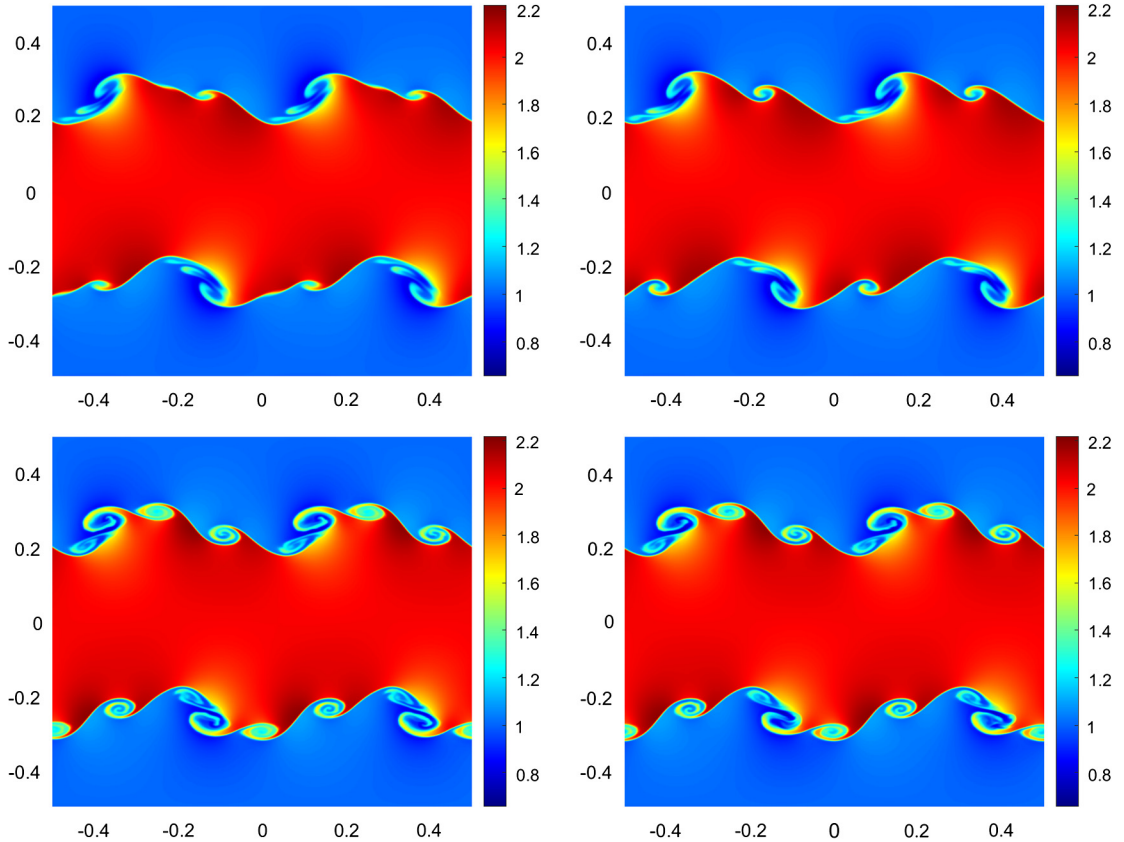


Fig. 4.10. Example 7: Density (ρ) computed by the CU (top left), Switch CU (top right), CURH-WS (bottom left), and CURH (bottom right) schemes at time $t = 1$.

Example 7 (Kelvin-Helmholtz (KH) instability). In this example, taken from [33] and also studied in [5,18], we investigate the ability of all of the studied schemes to capture the KH instability. To this end, we consider the following initial data:

$$(\rho(x, y, 0), u(x, y, 0)) = \begin{cases} (1, -0.5 + 0.5e^{(y+0.25)/L}), & y \in [-0.5, -0.25], \\ (2, 0.5 - 0.5e^{(-y-0.25)/L}), & y \in [-0.25, 0], \\ (2, 0.5 - 0.5e^{(y-0.25)/L}), & y \in [0, 0.25], \\ (1, -0.5 + 0.5e^{(0.25-y)/L}), & y \in [0.25, 0.5], \end{cases}$$

$$v(x, y, 0) = 0.01 \sin(4\pi x), \quad p(x, y, 0) = 1.5,$$

where L is a smoothing parameter, and we take $L = 0.00625$, which corresponds to a thin shear interface in the simulation below.

The computation domain is $[-0.5, 0.5] \times [-0.5, 0.5]$. We use a uniform grid with $\Delta x = \Delta y = 1/1024$ and the periodic boundary conditions to compute the solutions until the final time $t = 4$. The densities at times $t = 1, 2.5$, and 4 , computed by all of the studied schemes, are plotted in Figs. 4.10–4.12. As one can see in Fig. 4.10, the swirl structures produced by the CURH-WS and CURH schemes at $t = 1$ are much more clear than the similar structures in the CU and Switch CU solutions. Likewise, at the later times $t = 2.5$ and $t = 4$, the difference in the performance of the CURH-WS and CURH schemes compared to the CU and Switch CU schemes becomes more and more pronounced, as shown in Figs. 4.11 and 4.12, respectively. Notice that the CURH-WS and CURH schemes effectively resolve small details in the wave-breaking pattern and produce more isolated and complicated vorticities indicating that both of these two schemes can capture the KH instability much better than the CU and Switch CU schemes. On the other hand, in this example, we cannot find obvious difference between the CURH-WS and CURH schemes; see bottom rows of Figs. 4.10–4.12. This indicates that the numerical dissipation switch mechanism plays a lesser role here.

Example 8 (Raleigh-Taylor (RT) instability). In the final example, we numerically investigate the RT instability, which is a standard test for comparing the amount of numerical dissipation present in shock-capturing numerical schemes. Instead of (3.8), we numerically solve the 2-D Euler equations with gravitation acting downward in the y -direction:

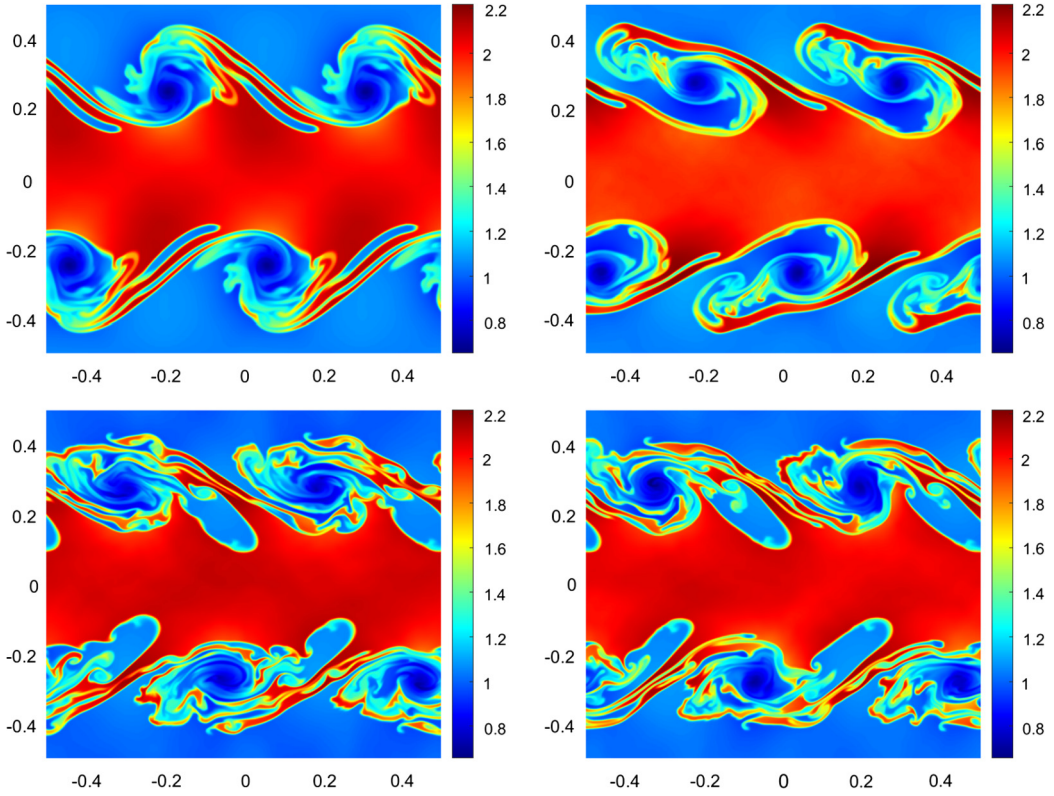


Fig. 4.11. Example 7: Density (ρ) computed by the CU (top left), Switch CU (top right), CURH-WS (bottom left), and CURH (bottom right) schemes at time $t = 2.5$.

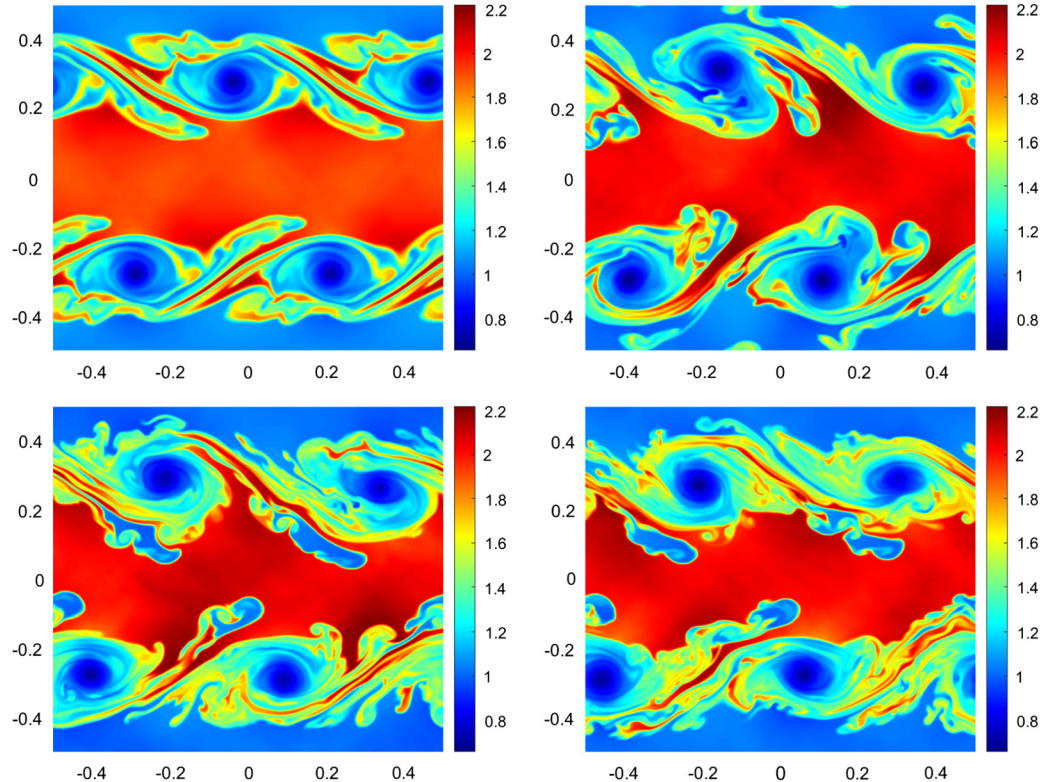


Fig. 4.12. Example 7: Density (ρ) computed by the CU (top left), Switch CU (top right), CURH-WS (bottom left), and CURH (bottom right) schemes at time $t = 4$.

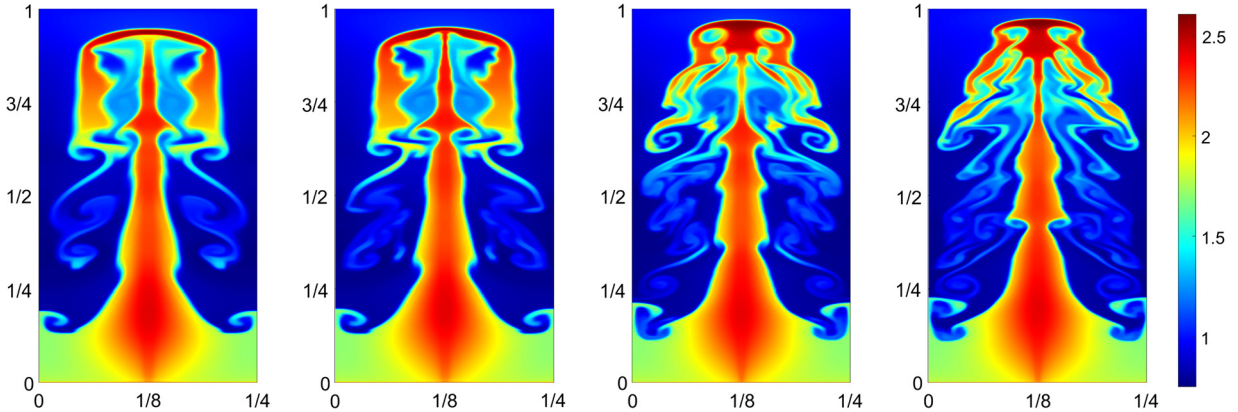


Fig. 4.13. Example 8: Density (ρ) computed by the CU, Switch CU, CURH-WS and CURH (from left to right) schemes.

$$\begin{aligned} \rho_t + (\rho u)_x + (\rho v)_y &= 0, \\ (\rho u)_t + (\rho u^2 + p)_x + (\rho u v)_y &= 0, \\ (\rho v)_t + (\rho u v)_x + (\rho v^2 + p)_y &= \rho v, \\ E_t + [u(E + p)]_x + [v(E + p)]_y &= \rho v. \end{aligned}$$

We use the setting from [38] and consider the following initial conditions:

$$(\rho(x, y, 0), u(x, y, 0), v(x, y, 0), p(x, y, 0)) = \begin{cases} (2, 0, -0.025 c \cos(8\pi x), 2y + 1), & y < 0.5, \\ (1, 0, -0.025 c \cos(8\pi x), y + 1.5), & \text{otherwise}, \end{cases}$$

where c is the speed of sound. The computational domain is $[0, 1/4] \times [0, 1]$. We impose the reflective (solid wall) boundary conditions at $x = 0$ and $x = 1/4$ and the Dirichlet boundary conditions at the top and bottom boundaries,

$$(\rho, u, v, p) \Big|_{y=1} \equiv (1, 0, 0, 2.5) \quad \text{and} \quad (\rho, u, v, p) \Big|_{y=0} \equiv (2, 0, 0, 1),$$

respectively.

We compute the solution until the final time $t = 2.95$ using a uniform mesh with $\Delta x = \Delta y = 1/1024$. The densities computed by all of the studied schemes are shown in Fig. 4.13. As one can see, the CURH scheme achieves a much better resolution of the complicated solution structures, which clearly indicates that the CURH scheme is less dissipative than the CU, Switch CU and CURH-WS ones.

5. Conclusion

In this paper, we have developed new semi-discrete central-upwind Rankine-Hugoniot (CURH) schemes. Compared with the original central-upwind schemes, the CURH schemes have a smaller amount of numerical dissipation. In order to achieve this goal, we employ two techniques: one depends upon the efficient use of discrete Rankine-Hugoniot conditions for the system of hyperbolic conservation laws, and the other is a numerical dissipation switch mechanism. These approaches are utilized in such a manner so that the amount of numerical dissipation can be controlled to a greater extent, particularly in the areas of contact waves and shear layers without compromising the robustness of the original central-upwind schemes. This fact is demonstrated through a number of challenging test problems for both one- and two-dimensional Euler equations of gas dynamics. The proposed CURH schemes not only lead to an improved resolution of contact waves, but also capture large-scale structures of the solutions in a much more accurate way.

CRediT authorship contribution statement

Naveen Kumar Garg: Conceptualization, Investigation, Methodology, Writing – original draft, Writing – review & editing. **Alexander Kurganov:** Conceptualization, Funding acquisition, Methodology, Project administration, Software, Supervision, Validation, Writing – original draft, Writing – review & editing. **Yongle Liu:** Conceptualization, Investigation, Methodology, Software, Validation, Visualization, Writing – original draft, Writing – review & editing.

Declaration of competing interest

The authors declare that they have no known competing financial interests or personal relationships that could have appeared to influence the work reported in this paper.

Acknowledgements

The work of A. Kurganov was supported in part by NSFC grant 11771201 and by the fund of the Guangdong Provincial Key Laboratory of Computational Science and Material Design (No. 2019B030301001).

References

- [1] P. Arminjon, A. St-Cyr, A. Madrane, New two- and three-dimensional non-oscillatory central finite volume methods on staggered Cartesian grids, *Appl. Numer. Math.* 40 (2002) 367–390.
- [2] P. Arminjon, M.-C. Viallon, A. Madrane, A finite volume extension of the Lax-Friedrichs and Nessyahu-Tadmor schemes for conservation laws on unstructured grids, *Int. J. Comput. Fluid Dyn.* 9 (1997) 1–22.
- [3] M. Ben-Artzi, J. Falcovitz, *Generalized Riemann Problems in Computational Fluid Dynamics*, Cambridge Monographs on Applied and Computational Mathematics, vol. 11, Cambridge University Press, Cambridge, 2003.
- [4] F. Bianco, G. Puppo, G. Russo, High order central schemes for hyperbolic systems of conservation laws, *SIAM J. Sci. Comput.* 21 (1999) 294–322.
- [5] U.S. Fjordholm, S. Mishra, E. Tadmor, On the computation of measure-valued solutions, *Acta Numer.* 25 (2016) 567–679.
- [6] N.K. Garg, S.V. Raghurama Rao, M. Sekhar, Weak-strong hyperbolic splitting for simulating conservation laws, *Int. J. Adv. Eng. Sci. Appl. Math.* 7 (2015) 62–69.
- [7] E. Godlewski, P.-A. Raviart, *Numerical Approximation of Hyperbolic Systems of Conservation Laws*, Applied Mathematical Sciences, vol. 118, Springer-Verlag, New York, 1996.
- [8] S.K. Godunov, A difference method for numerical calculation of discontinuous solutions of the equations of hydrodynamics, *Mat. Sb. (N.S.)* 47 (89) (1959) 271–306.
- [9] S. Gottlieb, D. Ketcheson, C.-W. Shu, *Strong Stability Preserving Runge-Kutta and Multistep Time Discretizations*, World Scientific Publishing Co. Pte. Ltd., Hackensack, NJ, 2011.
- [10] S. Gottlieb, C.-W. Shu, E. Tadmor, Strong stability-preserving high-order time discretization methods, *SIAM Rev.* 43 (2001) 89–112.
- [11] J.-L. Guermond, B. Popov, Fast estimation from above of the maximum wave speed in the Riemann problem for the Euler equations, *J. Comput. Phys.* 321 (2016) 908–926.
- [12] J.S. Hesthaven, Numerical methods for conservation laws, in: *From Analysis to Algorithms*, in: *Computational Science & Engineering*, vol. 18, Society for Industrial and Applied Mathematics (SIAM), Philadelphia, PA, 2018.
- [13] S. Jaisankar, S.V. Raghurama Rao, A central Rankine-Hugoniot solver for hyperbolic conservation laws, *J. Comput. Phys.* 228 (2009) 770–798.
- [14] G.-S. Jiang, E. Tadmor, Nonoscillatory central schemes for multidimensional hyperbolic conservation laws, *SIAM J. Sci. Comput.* 19 (1998) 1892–1917 (electronic).
- [15] D. Kröner, *Numerical Schemes for Conservation Laws*, Wiley-Teubner Series Advances in Numerical Mathematics, John Wiley & Sons Ltd., Chichester, 1997.
- [16] A. Kurganov, Central schemes: a powerful black-box solver for nonlinear hyperbolic PDEs, in: *Handbook of Numerical Methods for Hyperbolic Problems*, in: Handb. Numer. Anal., vol. 17, Elsevier/North-Holland, Amsterdam, 2016, pp. 525–548.
- [17] A. Kurganov, C.-T. Lin, On the reduction of numerical dissipation in central-upwind schemes, *Commun. Comput. Phys.* 2 (2007) 141–163.
- [18] A. Kurganov, Y. Liu, V. Zeitlin, Numerical dissipation switch for two-dimensional central-upwind schemes, *Modél. Math. Anal. Numér.* (2020), submitted for publication.
- [19] A. Kurganov, Y. Liu, V. Zeitlin, Thermal vs isothermal rotating shallow water equations: comparison of dynamical processes in two models by simulations with a novel well-balanced central-upwind scheme, *Geophys. Astrophys. Fluid Dyn.* 0 (2020) 1–30.
- [20] A. Kurganov, S. Noelle, G. Petrova, Semidiscrete central-upwind schemes for hyperbolic conservation laws and Hamilton-Jacobi equations, *SIAM J. Sci. Comput.* 23 (2001) 707–740.
- [21] A. Kurganov, M. Prugger, T. Wu, Second-order fully discrete central-upwind scheme for two-dimensional hyperbolic systems of conservation laws, *SIAM J. Sci. Comput.* 39 (2017) A947–A965.
- [22] A. Kurganov, E. Tadmor, New high-resolution central schemes for nonlinear conservation laws and convection-diffusion equations, *J. Comput. Phys.* 160 (2000) 241–282.
- [23] A. Kurganov, E. Tadmor, Solution of two-dimensional Riemann problems for gas dynamics without Riemann problem solvers, *Numer. Methods Partial Differ. Equ.* 18 (2002) 584–608.
- [24] P.D. Lax, X.-D. Liu, Solution of two-dimensional Riemann problems of gas dynamics by positive schemes, *SIAM J. Sci. Comput.* 19 (1998) 319–340 (electronic).
- [25] R.J. LeVeque, *Finite Volume Methods for Hyperbolic Problems*, Cambridge Texts in Applied Mathematics, Cambridge University Press, Cambridge, 2002.
- [26] D. Levy, G. Puppo, G. Russo, Central WENO schemes for hyperbolic systems of conservation laws, *Modél. Math. Anal. Numér.* 33 (1999) 547–571.
- [27] D. Levy, G. Puppo, G. Russo, Compact central WENO schemes for multidimensional conservation laws, *SIAM J. Sci. Comput.* 22 (2000) 656–672 (electronic).
- [28] D. Levy, G. Puppo, G. Russo, A fourth-order central WENO scheme for multidimensional hyperbolic systems of conservation laws, *SIAM J. Sci. Comput.* 24 (2002) 480–506.
- [29] K.-A. Lie, S. Noelle, On the artificial compression method for second-order nonoscillatory central difference schemes for systems of conservation laws, *SIAM J. Sci. Comput.* 24 (2003) 1157–1174.
- [30] R. Liska, B. Wendroff, Comparison of several difference schemes on 1d and 2d test problems for the Euler equations, *SIAM J. Sci. Comput.* 25 (2003).
- [31] X.-D. Liu, E. Tadmor, Third order nonoscillatory central scheme for hyperbolic conservation laws, *Numer. Math.* 79 (1998) 397–425.
- [32] H. Nessyahu, E. Tadmor, Nonoscillatory central differencing for hyperbolic conservation laws, *J. Comput. Phys.* 87 (1990) 408–463.
- [33] J. Panuelos, J. Wadsley, N. Kevlahan, Low shear diffusion central schemes for particle methods, *J. Comput. Phys.* 414 (2020) 109454.
- [34] J. Qiu, C.-W. Shu, On the construction, comparison, and local characteristic decomposition for high-order central WENO schemes, *J. Comput. Phys.* 183 (2002) 187–209.
- [35] S.V. Raghurama Rao, K. Balakrishna, An accurate shock capturing algorithm with a relaxation system for hyperbolic conservation laws, in: *16th AIAA Computational Fluid Dynamics Conference*, 2003, AIAA Paper, AIAA-2003-4115.
- [36] C.W. Schulz-Rinne, Classification of the Riemann problem for two-dimensional gas dynamics, *SIAM J. Math. Anal.* 24 (1993) 76–88.
- [37] C.W. Schulz-Rinne, J.P. Collins, H.M. Glaz, Numerical solution of the Riemann problem for two-dimensional gas dynamics, *SIAM J. Sci. Comput.* 14 (1993) 1394.
- [38] J. Shi, Y.-T. Zhang, C.-W. Shu, Resolution of high order WENO schemes for complicated flow structures, *J. Comput. Phys.* 186 (2003) 690–696.

- [39] P.K. Sweby, High resolution schemes using flux limiters for hyperbolic conservation laws, SIAM J. Numer. Anal. 21 (1984) 995–1011.
- [40] B. van Leer, Towards the ultimate conservative difference scheme. V. A second-order sequel to Godunov's method, J. Comput. Phys. 32 (1979) 101–136.
- [41] B.S. Wang, W.S. Don, N.K. Garg, A. Kurganov, Fifth-order A-WENO finite-difference schemes based on a new adaptive diffusion central numerical flux, SIAM J. Sci. Comput. 42 (2020) A3932–A3956.
- [42] Y. Zheng, Systems of conservation laws, in: Two-Dimensional Riemann Problems, in: Progress in Nonlinear Differential Equations and Their Applications, vol. 38, Birkhäuser Boston, Inc., Boston, MA, 2001.